

# Use of the ultraviolet absorption spectrum of $\text{CF}_2$ to determine the spatially resolved absolute $\text{CF}_2$ density, rotational temperature, and vibrational distribution in a plasma etching reactor

Nicolas Bulcourt and Jean-Paul Booth

*Laboratoire de Physique et Technologie des Plasmas (LPTP), Ecole Polytechnique, Palaiseau, France*

Eric A. Hudson and Jorge Luque

*Lam Research Corp., Fremont, California 94538*

Daniel K. W. Mok

*Department of Applied Biology and Chemical Technology, The Hong Kong Polytechnic University, Hung Hom, Hong Kong*

Edmond P. Lee

*Department of Applied Biology and Chemical Technology, The Hong Kong Polytechnic University, Hung Hom, Hong Kong, and Department of Chemistry, University of Southampton, Highfield, Southampton, SO17 1BJ, United Kingdom*

Foo-Tim Chau

*Department of Applied Biology and Chemical Technology, The Hong Kong Polytechnic University, Hung Hom, Hong Kong*

John M. Dyke<sup>a)</sup>

*Department of Chemistry, University of Southampton, Highfield, Southampton, SO17 1BJ, United Kingdom*

(Received 16 January 2004; accepted 13 February 2004)

Broadband ultraviolet absorption spectroscopy has been used to determine  $\text{CF}_2$  densities in a plasma etch reactor used for industrial wafer processing, using the  $\text{CF}_2 \tilde{A}^1B_1 \leftarrow \tilde{X}^1A_1$  absorption spectrum. Attempts to fit the experimental spectra using previously published Franck–Condon factors gave poor results, and values for the higher vibrational levels of the  $\tilde{A}$  state  $[(0, v_2, 0), \text{ with } v_2 > 6]$  from the ground state were missing; hence new values were calculated. These were computed for transitions between low-lying vibrational levels of  $\text{CF}_2 \tilde{X}^1A_1$  to vibrational levels of  $\text{CF}_2 \tilde{A}^1B_1 (v'_1, v'_2, 0)$  up to high values of the vibrational quantum numbers using high level *ab initio* calculations combined with an anharmonic Franck Condon factor method. The Franck Condon factors were used to determine the absorption cross sections of  $\text{CF}_2$  at selected wavelengths, which in turn were used to calculate number densities from the experimental spectra. Number densities of  $\text{CF}_2$  have been determined in different regions of the plasma, including the center of the plasma and outside the plasma volume, and  $\text{CF}_2$  rotational temperatures and vibrational energy distributions were estimated. For absorption spectra obtained outside the confined plasma volume, the  $\text{CF}_2$  density was determined as  $(0.39 \pm 0.08) \times 10^{13} \text{ molecule cm}^{-3}$  and the vibrational and rotational temperatures were determined as 303 and 350 K, respectively. In the center of the plasma reactor, the  $\text{CF}_2$  density is estimated as  $(3.0 \pm 0.6) \times 10^{13} \text{ molecules cm}^{-3}$  with  $T_{\text{rot}} \approx 500 \text{ K}$ . The fitted vibrational distribution in the  $\text{CF}_2$  ground state corresponds to two Boltzmann distributions with  $T_{\text{vib}} \approx 300$  and  $T_{\text{vib}} \approx 1000 \text{ K}$ , indicating that  $\text{CF}_2$  molecules are initially produced highly vibrationally excited, but are partially relaxed in the plasma by collision. © 2004 American Institute of Physics. [DOI: 10.1063/1.1695313]

## I. INTRODUCTION

Small reactive molecules such as  $\text{CF}_2$  play important roles in determining the etch rate, selectivity, and anisotropy of plasma etching processes. Absolute density measurements of these reactive molecules with spatial resolution are needed to test models of the chemistry of these systems and to optimize and control reactor performance.

Plasmas based on fluorocarbon-containing gas mixtures

are used for a variety of material processing applications, including the etching of thin films, deposition of fluorinated polymers, and chamber-wall cleaning after thin film deposition. Most notably, fluorocarbon plasmas are widely used to etch patterns into dielectric films, as required for the fabrication of integrated circuits on silicon wafers. A number of different dielectric etch applications have very stringent requirements, including high etch selectivity to photoresist and substrate films, tight control of etched feature profile and dimensions, uniform performance across the wafer surface, and highly repeatable etch results. In fact, these etch appli-

<sup>a)</sup>Corresponding author. Electronic mail: jmdyke@soton.ac.uk

cations represent some of the major challenges in the advancement of integrated circuit manufacturing technology, especially as feature dimensions decrease and wafer size increases to 300 mm.

Chemical pathways in fluorocarbon plasmas are complex, governed by a variety of interacting reaction types that may include dissociation, recombination, bimolecular exchange reactions, ionization, neutralization, film etch, and film deposition.  $\text{CF}_x$  species, with  $x=1-3$ , play important roles in determining the final etch results.  $\text{CF}_2$ , in particular, is often a principal carbon-bearing component in the plasma. This species has been studied extensively in fluorocarbon plasmas, and has shown complex behavior.<sup>1-3</sup> For example,  $\text{CF}_2$  spatial distributions have shown evidence of surface generation under some conditions.<sup>1-6</sup>  $\text{CF}_2$  is always present in high concentrations in the relatively fluorine-poor regimes produced by unsaturated fluorocarbon gases, which are typically used for highly selective etching of silicon dioxide films. Under these conditions  $\text{CF}_2$  has been proposed to act as a monomer in the formation of oligomeric species, which ultimately control polymer deposition.<sup>6,7</sup> Deposited fluorocarbon polymers provide control of etch selectivity, and of the profile and dimensions of the etched feature. The ability to accurately measure  $\text{CF}_2$  densities in plasmas is a valuable tool in the effort to understand critical plasma etch mechanisms and extend the capabilities of etch technology.

Several methods are commonly used to measure densities of reactive intermediates in processing-type plasmas, including Laser-Induced Fluorescence Spectroscopy (LIF),<sup>2-8</sup> Infra-Red Laser Absorption Spectroscopy,<sup>2</sup> and Ultraviolet Absorption Spectroscopy (UVAS). Of these, broadband UVAS has been used by a number of groups to detect  $\text{CF}_2$ .<sup>4,6-13</sup> The  $\text{CF}_2 \tilde{A} \leftarrow \tilde{X}$  transition in the  $\sim 225-275$  nm spectral range has a large peak absorbance under typical etch conditions. UVAS has several advantages, including a relatively low cost and simplicity of an experimental setup, the ability to measure ground-state vibrational and rotational distributions, and the possibility of measuring absolute densities. Disadvantages include the line-integrated nature of the measurement, which greatly complicates spatially resolved measurements, and the experimental challenge of accurately measuring the absorption coefficient over a wide spectral range. In principal, the line-integrated density of  $\text{CF}_2$  is easily determined from the measured intensity of the  $\tilde{A} (0n0) \leftarrow \tilde{X} (000)$  transitions, which is related to the density of  $\text{CF}_2$  in the plasma ground electronic and vibrational state. However, the situation is complicated by rotational broadening, which even at room temperature overlaps transitions to individual vibrational final states and may contribute to a continuum background absorption. Furthermore, if there is significant population of excited vibrational states in the ground electronic state, the resulting hot bands overlap with the fundamental transitions. Both of these effects complicate the extraction of reliable densities. In this paper we address these difficulties by presenting new experimental spectra for the  $\text{CF}_2 \tilde{A} \leftarrow \tilde{X}$  transition and comparing them to simulated spectra based upon new calculations of Franck-Condon factors [ $Q_{v',v''}$ 's, where  $v'$  is used as shorthand for  $(v'_1, v'_2, v'_3)$ , the

vibrational level of the  $\tilde{A}$  state, and similarly  $v''$  for the ground state]. Initial attempts to simulate the absorption spectra using the Franck-Condon factors determined by King, Schenck, and Stephenson<sup>14</sup> were in only moderate agreement with our experimental results, motivating the new calculations following the method outlined in our recent work.<sup>15</sup> To our knowledge, this is the first measurement of  $\text{CF}_2$  densities in a plasma that accounts for variations in initial state vibrational and rotational temperatures.

Recently, we have reported simulated spectra of the  $\tilde{A} \ ^1B_1 \rightarrow \tilde{X} \ ^1A_1$   $\text{CF}_2$  single vibronic level (SVL) emission, employing an *ab initio*/anharmonic Franck-Condon factor method.<sup>15</sup> This uses an anharmonic oscillator model and includes Duschinsky rotation. It involves calculating potential surfaces for the  $\tilde{X}$  and  $\tilde{A}$  electronic states using a high level *ab initio* method and fitting the computed potentials to an appropriate polynomial in symmetric bending and stretching coordinates. Vibrational wave functions obtained from these fitted potentials are then used to calculate Franck-Condon factors. In the simulation of the  $\tilde{A} \rightarrow \tilde{X}$  SVL spectra,<sup>15</sup> the simulated spectra obtained were found to be significantly superior to those obtained using a harmonic oscillator model<sup>16</sup> when compared with the experimental spectra. It is proposed to use this method to simulate the vibrationally resolved  $\tilde{A} \leftarrow \tilde{X}$  absorption spectrum recorded in a plasma etch reactor to estimate the vibrational and rotational state populations in the ground electronic state and determine number densities.

## II. EXPERIMENT

Reactive species were generated in a plasma using a modified 2300 Exelan<sup>®</sup> commercial dielectric etch system (Lam Research Corp., Fremont, CA). This etch reactor is designed for industrial wafer processing, primarily using fluorocarbon-based gas chemistry, and was configured for 200 mm wafers. The plasma is produced using a combination of 2 and 27 MHz radio-frequency (rf) excitation, capacitively coupled through the wafer, and is confined to a cylindrical volume using quartz rings. For these experiments, the vacuum chamber was modified with wider viewports to allow optical access over the full width of the cylindrical plasma volume. Fused silica viewports provided high transmission of UV radiation for  $>190$  nm.  $\text{CF}_2$  molecules were produced using a mixture of cyclo-octofluorobutane ( $c\text{-C}_4\text{F}_8$ ), oxygen, and argon as the feed gas. The feed gas is supplied to the confined region via a shower head in the reactor roof, and evacuated radially via gaps between the quartz confinement rings. The region outside the confinement rings is pumped with a turbomolecular pump; this region contains flowing gas at about 5 mTorr pressure (including etch products and the more stable reactive molecules), but no plasma. The total rf power was 3000 W and the plasma pressure was 55 mTorr. A silicon wafer was present in the reactor during the measurements, kept at a temperature of 293 K. The other surfaces in contact with the plasma can reach temperatures up to *ca.* 400 K.

A 150 W UV-enhanced Xe lamp (Oriel Instruments, Stratford, CT) equipped with a fused silica collimation lens

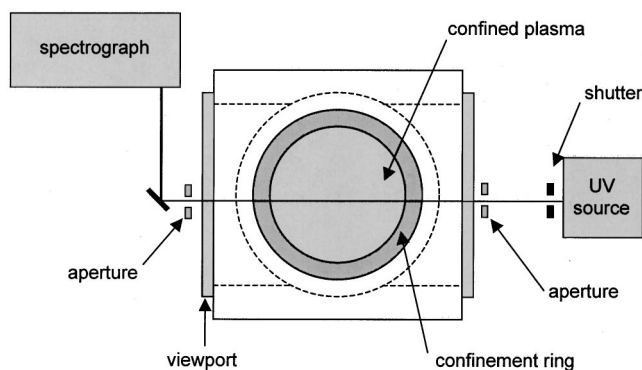


FIG. 1. Schematic of the experimental apparatus. In this arrangement, the beam traversed the centerline of the chamber, including a segment through the confined plasma volume.

was used as the UV source for the absorption experiments. The radiation was directed through a 1.5 mm high  $\times$  6 mm wide beam-defining aperture before entering the chamber. Two different optical layouts were used to measure absorption spectra. To measure species in the plasma, as shown in Fig. 1, the UV beam traversed the centerline of the chamber, including the plasma volume, in a horizontal plane lying just above the wafer. Alternatively, as shown in Fig. 2, the UV beam did not pass through the plasma. Instead two prisms were installed inside the vacuum chamber to direct the beam in a horizontal plane, along a 37 cm path through the outer region of the chamber. This arrangement ensures that the beam does not traverse the confined plasma volume, providing several advantages. Most importantly, the CF<sub>2</sub> species detected in the outer volume have a lower gas temperature than CF<sub>2</sub> molecules in the plasma, which simplifies the analysis of the spectra. In addition, the relative contribution to the spectrum from the CF radical<sup>17,18</sup> is reduced by this arrangement, since CF is more reactive than CF<sub>2</sub> and therefore has much lower densities outside the plasma volume. Finally, this arrangement avoids the collection of plasma optical emission by the detection optics, simplifying the measurement of the absorption spectrum.

After leaving the chamber, the radiation passed through another 1.5 mm  $\times$  6 mm aperture. A series of UV-grade mirrors rotated the image and directed the beam into a fused

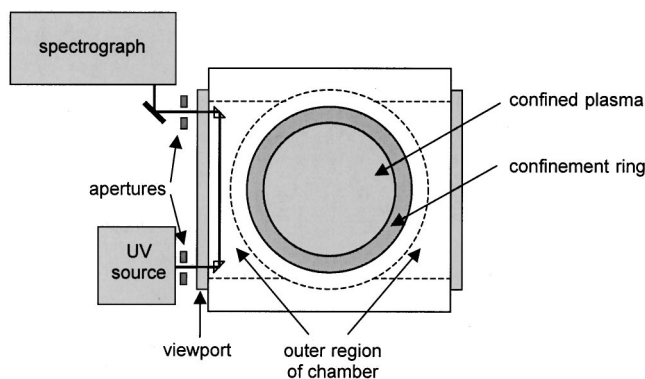


FIG. 2. Schematic of the experimental apparatus. In this alternative arrangement, the beam passes only through the outer region of the chamber, avoiding the confined plasma volume.

silica condensing lens, focused on the entrance slit of the spectrograph. The spectrograph was a 0.75 m modified Czerny–Turner type (Acton Research, Acton, CT) equipped with a 100  $\mu$ m entrance slit, 300 line/mm grating, and a 1024-element photodiode array detector (Andor Instruments, Belfast, Northern Ireland). Under these conditions, the spectral resolution was 0.45 nm (FWHM). The multichannel detection system allowed spectral detection over a wide wavelength range without scanning. This is an essential capability for broadband absorption spectroscopy, where small fluctuations in the source intensity can greatly affect the derived absorption spectrum.

The measurement of absorption spectra for species present in a plasma is complicated by the optical emission signal from the plasma, which may be considerable under wafer processing conditions. This contribution is removed by making two separate measurements of the plasma-on spectrum: (1) with the photon source active to measure the transmitted beam plus optical emission; and (2) with the photon source blocked to measure plasma optical emission only. In addition, plasma-off measurements of the source spectrum are also required, to provide the  $I_0$  signal for the calculation of absorbance. A measurement of the detector background signal, with no photon source or plasma, is used to correct for the “dark” signal, which is due mainly to electrical offset in the detector. In practice, a single background spectrum is sufficient for a series of spectral measurements. The source spectrum was measured immediately before or after the plasma was produced, to minimize the systematic error arising from drift in the lamp output spectrum. With the plasma on, the optical emission signal was collected alternately with the transmitted beam in 5 s cycles, using an electronic shutter to alternately block and expose the source. The data collection is synchronized to the shutter, saving transmission and emission spectra to separate data buffers. The total plasma-on measurement time was 30 s.

The absorption spectrum for the arrangement where the UV beam passed through the plasma was calculated from the measured spectra by Eq. (1):

$$A = \text{Ln} \left( \frac{\text{source} - \text{background}}{(\text{source} + \text{plasma}) - \text{plasma emission}} \right) = \text{Ln} \left( \frac{I_0}{I} \right). \quad (1)$$

For the case when the UV beam did not pass through the plasma, there is no plasma emission correction, and the final absorbance is calculated from the measured spectra by Eq. (2):

$$A = \text{Ln} \left( \frac{\text{source} - \text{background}}{\text{sample} - \text{background}} \right) = \text{Ln} \left( \frac{I_0}{I} \right). \quad (2)$$

The Xe lamp had a much more intense output at visible wavelengths, compared to the UV. However, measurements with deep UV radiation filtered out showed that stray visible and near UV radiation made a negligible contribution to the spectrograph signal. Spectral wavelengths were calibrated using the neutral carbon atomic transition at 247.856 nm,<sup>19</sup> as detected in the plasma optical emission spectrum.

### III. THEORETICAL

#### A. *Ab initio*, rotational constant and Franck–Condon factor ( $Q_{\nu, \nu''}$ ) calculations

##### 1. A new *ab initio* potential energy function for the $\tilde{A}^1B_1$ state of $CF_2$

Since the observed absorption spectrum of  $CF_2$  consists of excitations to higher vibrational levels of the  $\tilde{A}^1B_1$  state than those involved in the SVL emission spectra studied previously,<sup>15</sup> a new potential energy function (PEF) for the  $\tilde{A}^1B_1$  state derived from an extended energy scan over both the bond length and angle coordinates is required. Extra CASSCF/MRCI/aug-cc-pVQZ(no *g*) energy calculations on the  $\tilde{A}^1B_1$  state were carried out, as described previously,<sup>15</sup> employing the MOLPRO suite of programs.<sup>20</sup> The CF bond length and FCF angle ranges of the new PEF are 1.00–1.75 Å and 80°–160°, respectively, giving 107 energy points on the  $\tilde{A}^1B_1$  state hypersurface (cf. 40 points used previously).<sup>15</sup> The new PEF,  $V$ , was determined by fitting the following polynomial to the 107 CASSCF/MRCI/aug-cc-pVQZ(no *g*) single-point energies of the  $\tilde{A}^1B_1$  state of  $CF_2$ , as described previously:<sup>15</sup>

$$V = \sum_{ij} C_{ij} (S_1)^i (S_2)^j + V_{eqm} \quad (3)$$

The PEF is expressed in terms of a Morse-type coordinate,<sup>21</sup>

$$S_1 = [1 - e^{-\gamma(r - r_{eqm})/r_{eqm}}] / \gamma, \quad (4)$$

and a bending coordinate suggested by Carter and Handy,<sup>22</sup>

$$S_2 = \Delta\theta + \alpha \Delta\theta^2 + \beta \Delta\theta^3, \quad (5)$$

where  $r$  is the CF bond length, and  $\Delta\theta$  is the displacement in the FCF bond angle. The PEF of the  $\tilde{X}^1A_1$  state used in the present study is the same as published previously for the simulation of the SVL emission spectra.<sup>15</sup> The coefficients of, and the equilibrium geometrical parameters, harmonic ( $\omega$ ) and fundamental ( $\nu$ ) vibrational constants from, the PEF of the  $\tilde{X}^1A_1$  state, and both the new and previously used<sup>15</sup> PEFs of the  $\tilde{A}^1B_1$  state are given in Table I. It can be seen from Table I that more higher-order terms were included in the new PEF of the  $\tilde{A}^1B_1$  state than previously,<sup>15</sup> and it should be more reliable than the PEF reported in Ref. 15. Nevertheless, the equilibrium geometrical parameters derived from the new and previously published PEFs for the  $\tilde{A}^1B_1$  state differ only slightly (by 0.0007 Å and 0.129° in  $r_e$  and  $\theta_e$ , respectively), suggesting that near the equilibrium region, the two PEFs are very similar.

##### 2. Anharmonic vibrational wave functions and rotational constants

Variational calculations of anharmonic vibrational wave functions were carried out for the  $\tilde{A}^1B_1$  state, employing the new PEF obtained in the present study, as described previously,<sup>15</sup> and hence only details specific to the present study are given here. Briefly, anharmonic vibrational wave functions were expressed as linear combinations of harmonic oscillator functions,  $h(v_1, v_2)$ , where  $v_1$  and  $v_2$  denote the quantum numbers of the harmonic basis functions for the

TABLE I. The coefficients of, and the equilibrium geometrical parameters from, the RCCSD(T)/aug-cc-pVQZ PEF of the  $\tilde{X}^1A_1$  state, and both the new and previously used CASSCF/MRCI/aug-cc-pVQZ(no *g*) PEFs of the  $\tilde{A}^1B_1$  state.

Parameters	$\tilde{X}^1A_1$ RCCSD(T)	$\tilde{A}^1B_1$ CASSCF/MRCI	New $\tilde{A}^1B_1$ CASSCF/MRCI
$C_{20}$	3.0469	2.7504	2.7793
$C_{11}$	0.3986	0.1350	0.1508
$C_{03}$	0.2710	0.1241	0.1238
$C_{30}$	-5.6472	10.6753	1.7522
$C_{21}$	-1.7372	-0.0997	-0.3174
$C_{12}$	-1.0191	-0.4177	-0.3800
$C_{03}$	-0.0698	-0.0213	0.0328
$C_{40}$	6.2001	48.4845	-1.4927
$C_{22}$	1.5673	-0.7977	-0.3538
$C_{04}$	0.2528	0.0373	0.0499
$C_{31}$	2.1408 <sup>a</sup>	0.6084 <sup>a</sup>	-1.1833
$C_{13}$	0.5872 <sup>a</sup>	0.2078 <sup>a</sup>	0.0304
$C_{05}$	0.1008	0.0984	-0.1035
$C_{06}$	-0.4663	0.3177	0.2242
$C_{50}$	-1.7222	148.2864	-19.4261
$C_{60}$	-3.2016	181.0831	-33.2809
$C_{41}$	-0.3516	3.6957	-4.8962
$C_{32}$	-1.5753	-0.9673	-2.5373
$C_{23}$	-1.8493	-0.4355	-0.9338
$C_{14}$	-0.8155	-0.4291	-0.3785
$C_{51}$	...	...	-6.2456
$C_{42}$	...	...	-4.0785
$C_{33}$	...	...	-1.5229
$C_{23}$	...	...	-0.3789
$C_{15}$	...	...	0.0633
$C_{07}$	-0.0887	...	0.7579
$C_{08}$	1.3159	...	0.5043
$C_{70}$	...	...	62.9150
$C_{80}$	...	...	172.8504
$r_{eqm}/\text{Å}$	1.3008	1.3215	1.3208
$\theta_{eqm}/^\circ$	104.754	121.980	122.109
$\alpha/\text{radi}^{-1}$	-0.0516	-0.1944	-0.1204
$\gamma$	1.3151	6.9581	4.0486
$\omega_1/\text{cm}^{-1}$	1242 <sup>b</sup>	1058 <sup>b</sup>	1057
$\nu_1/\text{cm}^{-1}$	1231 <sup>b</sup>	1042 <sup>b</sup>	1040
$\omega_2/\text{cm}^{-1}$	670 <sup>b</sup>	500 <sup>b</sup>	502
$\nu_2/\text{cm}^{-1}$	668 <sup>b</sup>	496 <sup>b</sup>	499

<sup>a</sup>Note that there were some typing errors in the PEFs of both the  $\tilde{X}^1A_1$  and  $\tilde{A}^1B_1$  states given in Ref. 15: The  $C_{31}$  and  $C_{13}$  coefficients were swapped. The correct values are given here ( $\omega$  and  $\nu$  represent harmonic and fundamental vibrational constants, respectively).

<sup>b</sup>From Ref. 15.

symmetric stretching and bending modes, respectively. The asymmetric  $\nu_3$  stretching mode was not considered—as both the  $\tilde{X}$  and  $\tilde{A}$  states have  $C_{2v}$  equilibrium structures; the excitations in  $\nu_3$  are therefore only allowed in double quanta and are expected to be very weak. Harmonic basis functions up to  $h(15,40)$ , with the restriction of  $v_1 + v_2 < 40$ , were included in the variational calculations [cf.  $h(10,15)$  and  $v_1 + v_2 < 15$  used previously<sup>15</sup>]. A larger variational calculation with harmonic basis functions up to  $(20,50)$  and  $v_1 + v_2 < 50$  was also carried out to check the adequacy of the size of the variational calculation. The differences in the computed anharmonic vibrational energies between employing the two harmonic basis sets are smaller than  $1 \text{ cm}^{-1}$  for vibrational levels with energies of up to  $7900 \text{ cm}^{-1}$  [around

the anharmonic vibrational level (2,12)], showing that the effect of any further increase in size on the variational calculation would be negligible.

The anharmonic vibrational wave functions obtained for the  $\tilde{A}^1B_1$  state, employing the new PEF, were used together with the anharmonic wave functions of the  $\tilde{X}^1A_1$  state reported previously<sup>15</sup> to calculate the  $Q_{v',v''}$ 's for simulations of first the SVL emission spectra<sup>14</sup> and then the absorption spectrum of CF<sub>2</sub> presented in this work, which will be discussed below.

Rotational constants of each vibrational level of interest were calculated from the average geometrical parameters, which are the expectation values of the bond length and angle calculated using the anharmonic vibrational wave function of that particular vibrational level ( $\langle r \rangle = \langle \Psi_{\text{vib}} | r | \Psi_{\text{vib}} \rangle$ ). Rotational constants thus obtained of the vibrational levels of both the  $\tilde{X}^1A_1$  and  $\tilde{A}^1B_1$  states involved in the absorption were used to simulate the rotational structure of the vibrational components of the absorption spectrum.

### 3. New IFCA geometry of the $\tilde{A}^1B_1$ state and Franck–Condon factors for the absorption spectrum of CF<sub>2</sub>

With the anharmonic vibrational wave functions obtained from the new PEF of the  $\tilde{A}^1B_1$  state, the iterative Franck–Condon analysis (IFCA) procedure was carried out to obtain the IFCA geometry of the  $\tilde{A}^1B_1$  state (with the geometry of the  $\tilde{X}^1A_1$  state fixed to the available experimental geometry; see Ref. 15). This involved changing the geometrical parameters of the  $\tilde{A}^1B_1$  state slightly until the best match between the simulated (a frequency factor of power four was used; see Ref. 15) and the observed SVL emission spectra<sup>14</sup> was obtained. The simulated and observed SVL emission spectra are, in general, in excellent agreement with the new IFCA geometrical parameters of the  $\tilde{A}^1B_1$  state of CF<sub>2</sub> determined as  $r_e(\text{CF}) = 1.3177 \text{ \AA}$  and  $\theta_e(\text{FCF}) = 121.5^\circ$ , which compare very well with those reported previously (1.317 Å and 122.5°, respectively), using the less extended PEF of the  $\tilde{A}^1B_1$  state.<sup>15</sup>

Other than matching the simulated spectra with the observed spectra given in Ref. 14, an attempt was also made to match our calculated  $Q_{v',v''}$ 's with the  $Q_{v',v''}$ 's given therein, derived from the observed spectra, taking into account the detector efficiency. A good overall agreement is obtained for the  $\tilde{A}(000) \rightarrow \tilde{X}$  SVL emission with the IFCA geometry of the  $\tilde{A}^1B_1$  state given above. For other reported SVL emissions<sup>14</sup> from higher vibrational levels of the  $\tilde{A}^1B_1$  state, good agreement between the derived  $Q_{v',v''}$ 's<sup>14</sup> and our calculated values is obtained only for vibrational components that emit to the lower vibrational levels (*ca.*  $v''_2 \leq 5$ ) of the ground electronic state of CF<sub>2</sub>. However, for emission to higher vibrational levels of the ground state, the computed  $Q_{v',v''}$ 's are smaller than the experimentally derived  $Q_{v',v''}$ 's given in Ref. 14. Nevertheless, it should be noted that the experimental intensities of the vibrational components and the quoted uncertainties of the derived  $Q_{v',v''}$ 's in Ref. 14, involving higher vibrational levels of the ground electronic

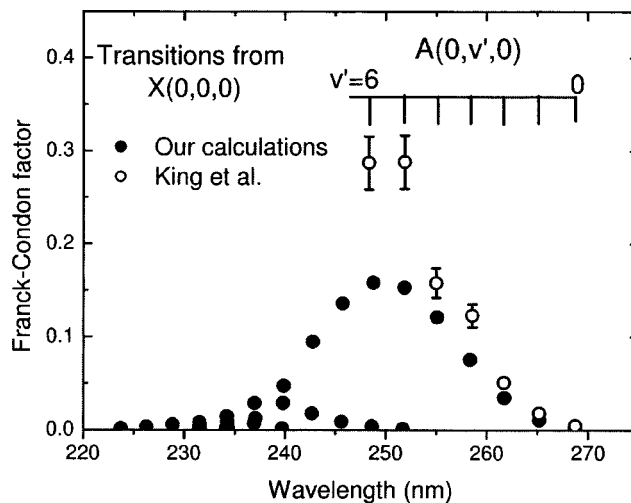


FIG. 3. Calculated Franck–Condon factors (see Table II) for transitions from  $\tilde{X}(0,0,0)$  compared with the values of King *et al.* (Ref. 14).

state, are generally weaker and larger, respectively, than those of low vibrational levels. It is also noted that for simulating the absorption spectrum, only  $Q_{v',v''}$ 's involving low vibrational levels of the ground electronic state are required. Therefore, we are confident that the computed  $Q_{v',v''}$ 's employing the new PEF and the new IFCA geometry of the  $\tilde{A}^1B_1$  state reported in the present study are adequate for the simulation of the absorption spectrum of CF<sub>2</sub>. A more quantitative comparison between the *ab initio* and experimentally derived  $Q_{v',v''}$  values<sup>14</sup> will be discussed below.

Figures 3 and 4 show our calculated Franck–Condon factors for transitions from  $\tilde{X}(0,0,0)$  and  $\tilde{X}(0,1,0)$ , respectively. Also shown are the values from King *et al.*<sup>14</sup> Table II gives the numerical values for the stronger transitions ( $Q_{v',v''} > 10^{-3}$ ). Below 250 nm, there are a number of nearly degenerate transitions, due to the comparable values of two quanta of  $\nu'_2$  with one quantum of  $\nu'_1$ . Indeed, the levels become mixed, and it is not possible to attribute exact vibrational designations: the attributions given in the table repre-

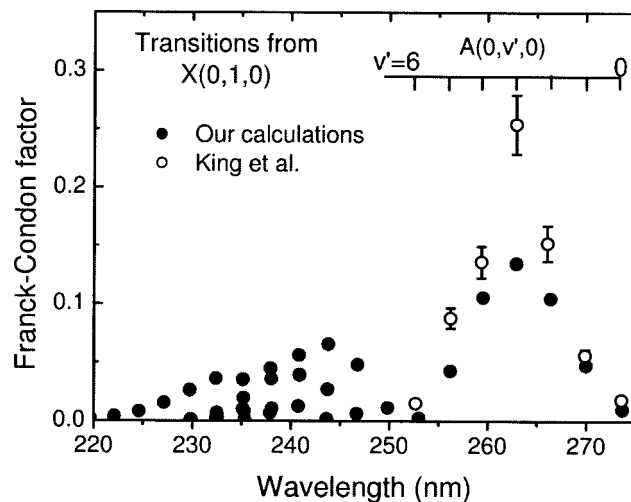


FIG. 4. Calculated Franck–Condon factors (see Table II) for transitions from  $\tilde{X}(0,1,0)$  compared with the values of King *et al.* (Ref. 14).

TABLE II. Franck–Condon factors and wavelengths for the strongest transitions from the  $\tilde{X}(0,0,0)$  and  $\tilde{X}(0,1,0)$  states obtained from the *ab initio* calculations in this work.<sup>a</sup>

A state ( $v_1', v_2', v_3'$ )	Transitions from $\tilde{X}(0,0,0)$		Transitions from $\tilde{X}(0,1,0)$	
	$\lambda$ (nm)	$Q_{v'v''}$	$\lambda$ (nm)	$Q_{v'v''}$
(0,0,0)	268.74	0.0015	273.65	0.0099
(0,1,0)	265.19	0.0104	269.97	0.0477
(0,2,0)	261.73	0.0347	266.39	0.1048
(0,3,0)	258.37	0.0754	262.91	0.1348
(0,4,0)	255.09	0.1211	259.52	0.1057
(0,5,0)	251.90	0.1530	256.21	0.0429
(0,6,0)	248.78	0.1581	252.99	0.0024
(1,4,0)	248.63	0.0038		
(0,7,0)	245.74	0.1357	249.85	0.0114
(1,5,0)	245.62	0.0089		
(0,8,0)	242.78	0.0947	246.78	0.0482
(1,6,0)	242.69	0.0177	246.69	0.0063
(0,9,0)	239.89	0.0474	243.80	0.0655
(1,7,0)	239.82	0.0290	243.73	0.0269
(2,5,0)	239.73	0.0015	243.63	0.0017
(0,10,0)*	237.08	0.0126	240.90	0.0394
(0,10,0)*	237.02	0.0288	240.83	0.0563
(2,6,0)*	236.95	0.0072	240.77	0.0126
(1,8,0)	234.35	0.0013	238.08	0.0105
(2,6,0)*	234.28	0.0093	238.01	0.0359
(1,9,0)*	234.23	0.0148	237.95	0.0448
(3,6,0)	234.18	0.0025	237.90	0.0067
(1,9,0)*			235.35	0.0012
(2,7,0)			235.28	0.0079
(3,5,0)	231.57	0.0035	235.21	0.0196
(1,11,0)	231.52	0.0080	235.16	0.0354
(4,5,0)	231.49	0.0025	235.13	0.0101
(4,4,0)			232.56	0.0029
(3,8,0)			232.50	0.0067
(5,4,0)			232.46	0.0027
(1,12,0)	228.87	0.0061	232.42	0.0362
(6,3,0)*			229.87	0.0013
(6,3,0)*			229.86	0.0013
(0,15,0)	226.28	0.0033	229.76	0.0263
(0,16,0)	223.75	0.0015	227.15	0.0154
(0,17,0)			224.60	0.0081
(0,18,0)			222.11	0.0039
(0,19,0)			219.67	0.0017
Sum		0.9943		0.9951

<sup>a</sup>Shown in this table under the  $\tilde{A}$ -state heading (first column) are the harmonic basis functions with the largest computed coefficients in the corresponding anharmonic vibrational wavefunctions. The \*'s indicate anharmonic levels, which have strong mixing and have the same leading harmonic terms. Hence the vibrational designations (quantum numbers) of these anharmonic wave functions cannot be obtained from the leading harmonic terms (see the text).

sent the quantum numbers of the basis functions that have the strongest coefficients in each state. As a consequence, some vibrational state labels (marked with an asterisk) appear twice in the table.

Our calculated  $Q_{v'v''}$  values agree reasonably well with most experimentally derived values of King *et al.*,<sup>14</sup> except for the  $\tilde{A}(0,5,0) - \tilde{X}(0,0,0)$ ,  $\tilde{A}(0,6,0) - \tilde{X}(0,0,0)$ , and  $\tilde{A}(0,3,0) - \tilde{X}(0,1,0)$  transitions (see Figs. 3 and 4), where our calculated values are significantly smaller (by up to nearly a factor of 2) than the values of King *et al.*<sup>14</sup> This difference can be attributed primarily to the fact that King *et al.* neglected many of the higher vibrational levels of the  $\tilde{A}$  state,

TABLE III. Rotational constants for the  $\tilde{X}(v_1, v_2, 0)$  states obtained from the *ab initio* calculations in this work. The values for the first two levels are identical to the experimental values of Ref. 24.

X state	A (cm <sup>-1</sup> )	B (cm <sup>-1</sup> )	C (cm <sup>-1</sup> )
(0,0,0)	2.947 21	0.417 21	0.364 66
(0,1,0)	2.973 55	0.416 14	0.363 05
(1,0,0)	2.995 73	0.415 23	0.361 69
(0,2,0)	2.999 88	0.415 06	0.361 44
(1,1,0)	3.021 86	0.414 17	0.360 10
(0,3,0)	3.026 19	0.413 99	0.359 83
(2,0,0)	3.043 92	0.413 27	0.358 75
(1,2,0)	3.047 97	0.413 10	0.358 50
(0,4,0)	3.052 48	0.412 92	0.358 23
(0,5,0)	3.078 73	0.411 84	0.356 62
(0,6,0)	3.104 95	0.410 77	0.355 02

and noting the condition that the sum of the  $Q_{v'v''}$ 's from any vibronic level of the  $\tilde{X}$  state to all possible vibronic levels in the  $\tilde{A}$  state must be unity. This has a significant implication for absolute density measurements. A further significant difference is in the relative values of the  $Q_{v'v''}$  values from  $\tilde{X}(0,0,0)$  and  $\tilde{X}(0,1,0)$  in the 260–270 nm region, where pairs of isolated bands can be used to estimate the vibrational temperature. We were not able to fit our experimental spectra in this region using the values from King *et al.*,<sup>14</sup> suggesting that the  $Q_{v'v''}$ 's of King *et al.* are unreliable, almost certainly because of the deficiency described above. With our computed  $Q_{v'v''}$ 's, our simulated spectra provide more complete vibrational analyses of the observed spectra than those given in Ref. 14, and hence the full set of theoretical  $Q_{v'v''}$ 's obtained in this work is more reliable than the experimentally derived  $Q_{v'v''}$ 's of King *et al.*<sup>14</sup>

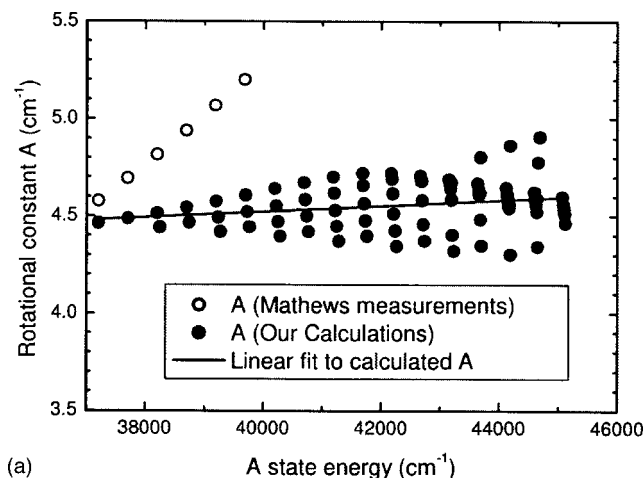
## B. Simulation of the CF<sub>2</sub> absorption spectra

The absorbance is related to the column density,  $nL$ , and the absorption cross-section by

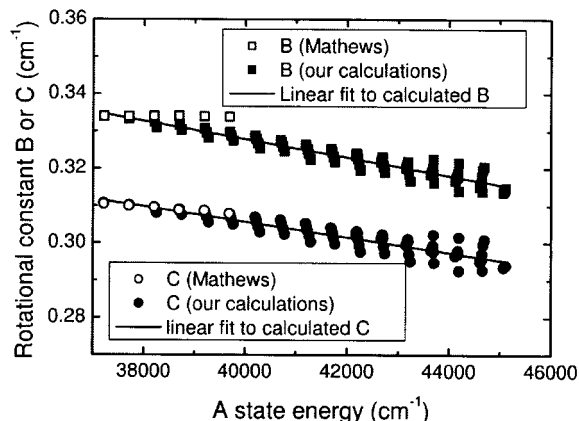
$$A(\lambda) = \sigma(\lambda)nL. \quad (6)$$

The absorption cross-sections for CF<sub>2</sub> were calculated in the following way. The rotational envelope for each vibronic transition,  $S_{v'v''}(T_{\text{rot}}, \lambda)$  was calculated using an asymmetric rotor spectral simulation program.<sup>23</sup> A Gaussian form for the spectrograph transmission function was assumed with a FWHM of 0.45 nm. Each envelope was normalized so that the integral over wavelength was equal to unity. The transition energies,  $T_{0(v'v'')}$ , and Franck–Condon factors,  $Q_{v'v''}$ , of each transition were taken from the *ab initio* calculations. As the experimental resolution is rather low, only the rotational constants  $A$ ,  $B$ , and  $C$  were considered in each state, and the centrifugal distortion terms  $D_J$ ,  $D_{JK}$ ,  $D_K$  were not included. The rotational constants for the  $\tilde{X}(0,0,0)$  and  $\tilde{X}(0,1,0)$  states (Table III) were taken from the gas-phase infrared work of Qian *et al.*<sup>24</sup> The rotational constants obtained for higher  $\tilde{X}(v_1', v_2'', 0)$  levels from the *ab initio* calculations are also shown in Table III.

The rotational constants for the  $\tilde{A}$  state have only been determined experimentally for the levels  $\tilde{A}(0, v_2', 0)$  with  $v_2' = 0-5$  from electronic absorption spectroscopy.<sup>25</sup> The rota-



(a)

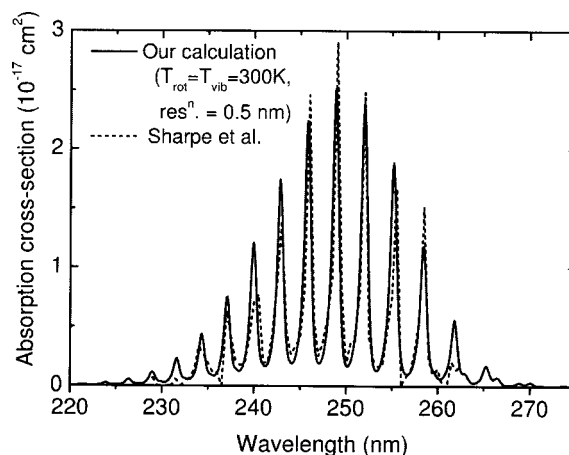


(b)

FIG. 5. The CF<sub>2</sub>  $\tilde{A}$  state rotational constants  $A$  (a), and  $B$  and  $C$  (b).

tional constants for the  $\tilde{A}$  state were also deduced from the *ab initio* calculations (see Table III), as described earlier. The calculated values extend to much higher values  $v'_2$ , and also include states with  $v'_1 \neq 0$  (although  $v'_3$  was not treated). Figures 5(a) and 5(b) show these constants as a function of the  $\tilde{A}$ -state energy. The spread of rotational constants for similar  $\tilde{A}$ -state energies is due to excitation of the symmetric stretching mode: increasing  $v'_1$  decreases the rotational constants somewhat due to the increase in the average bond length, whereas a molecule in the vibrational state  $((v'_1+1), (v'_2-2), 0)$  has only slightly more energy than a molecule in  $(v'_1, v'_2, 0)$ .

As can be seen from Figs. 5(a) and 5(b), the calculated  $\tilde{A}$ -state  $B$  and  $C$  constants are in reasonable agreement with the experimental measurements, whereas the  $A$  constant is in less good agreement. While we can see no obvious reason for these differences in the  $A$  constant and think that our calculations are reliable, it is possible that the CF<sub>2</sub> absorption spectrum recorded over 30 years ago<sup>25</sup> needs to be reinvestigated to clarify this point. However, the  $A$  constant has relatively little effect on the overall spectrum at the experimental resolution used. In order to simplify the spectral calculations, and considering the large number of vibrational levels involved and the relatively low experimental spectral resolution, the  $A$ ,  $B$  and  $C$  constants were expressed as linear functions of the  $\tilde{A}$ -state energy,  $T_{0(v')}$ , obtained by fitting a

FIG. 6. Calculated absorption cross-section for CF<sub>2</sub> at 300 K. Also shown is the experimental data of Sharpe *et al.* (Ref. 27). The calculated peak absorbance (at 249 nm) is only 16% lower than the value of Sharpe *et al.* (Ref. 27).

straight line to the *ab initio* values, as shown in Figs. 5(a) and 5(b). The absorption cross-section from a given vibrational level of the ground state was calculated from (17):

$$\sigma_{v''}(\lambda, T_{\text{rot}}) = C \sum_{v'} Q_{v', v''} \lambda_{v', v''} S_{v', v''}(T_{\text{rot}}, \lambda), \quad (7)$$

where  $S_{v', v''}(T_{\text{rot}}, \lambda)$  is the rotational intensity at wavelength  $\lambda$  for each vibronic transition, and  $\lambda_{v', v''}$  is the wavelength in nanometers of the transition  $\tilde{A}(v'_1, v'_2, v'_3) \leftarrow \tilde{X}(v''_1, v''_2, v''_3)$ . The factor  $\lambda_{v', v''}$ , which is the wavelength in nanometers of the transition  $\tilde{A}(v'_1, v'_2, v'_3) \leftarrow \tilde{X}(v''_1, v''_2, v''_3)$ , occurs because the spectra are recorded as a function of wavelength.<sup>17</sup>  $C$  is a normalization constant, defined such that

$$\int \frac{hc}{\lambda} \sigma_{v''}(\lambda, T_{\text{rot}}) d\lambda = \frac{2\pi^2}{3\epsilon_0} \frac{1}{g''} |R_{AX}|^2. \quad (8)$$

where  $R_{AX}$  is the electronic transition dipole moment. Its value was estimated from the  $\tilde{A}$ -state fluorescence lifetime ( $50 \pm 5$  ns<sup>26</sup>), giving a value of  $R_{AX} = 1.29$  Debye =  $4.3 \times 10^{-30}$  C m. It was assumed to be constant over the absorption band.

As, under experimental conditions, the ground state CF<sub>2</sub> molecules in the plasma will have a distribution over vibrational states,  $f_{v''}$ , the overall absorption cross-section is defined as

$$\sigma(\lambda, T_{\text{rot}}, f_{v''}) = C \sum_{v''} P_{v''} \sigma_{v''}(\lambda, T_{\text{rot}}), \quad (9)$$

where  $P_{v''}$  is the fraction of the ground state population in the vibrational level  $v''$ . If the system is in Boltzmann equilibrium, then  $P_{v''} = e^{-E_{v''}/kT_{\text{vib}}}$ .

Figure 6 shows the calculated absorption cross-section as a function of wavelength, assuming vibrational and rotational temperatures in equilibrium at 300 K, and a spectral resolution of 0.5 nm. Also shown is the experimental data of Sharpe *et al.*<sup>27</sup> The agreement is very good, the peak absorbance (at 249 nm) being only 16% lower than the value given by Sharpe *et al.*<sup>27</sup>

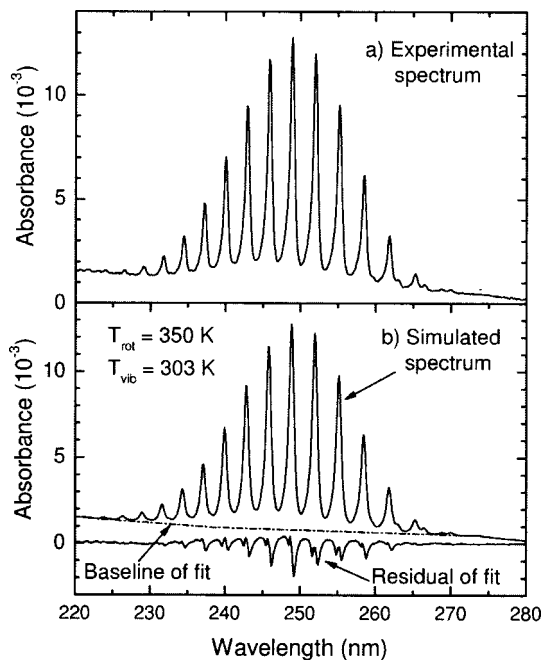


FIG. 7. (a) Experimental UV absorption spectrum of  $\text{CF}_2$  taken outside the confinement rings. (b) UV absorption spectrum of  $\text{CF}_2$  simulated to fit (a). The temperatures shown are the Boltzmann rotational and vibrational temperatures used to fit the experimental spectrum.

#### IV. EXPERIMENTAL RESULTS AND SPECTRAL SIMULATIONS

##### A. Spectra taken outside the confinement rings

Figure 7(a) shows an experimental absorption spectrum taken outside the confinement rings. In this region, where the gas is cold, the density of  $\text{CF}_2$  is not negligible, and must be taken into account for the study inside the plasma. It should be noted, however, that for the spectrum shown in Fig. 7(a), the  $\text{CF}_2$  density was increased further by throttling the turbo pump, giving a gas pressure of 29 mTorr: this was done in order to obtain a high-quality spectrum of cold  $\text{CF}_2$ , which would be a good test of the Franck–Condon factors (when the pump is operating at full speed the gas pressure in this region is only about 5 mTorr).

The experimental spectrum was fitted using a nonlinear least-squares fitting routine. The variable parameters in the fit were  $nL$ , the total column density of  $\text{CF}_2$  (with  $L$  defined by the experimental pathlength),  $T_{\text{rot}}$ , the rotational temperature, and the vibrational temperature,  $T_{\text{vib}}$ . In this case it was only necessary to consider the lowest two vibrational levels,  $\tilde{X}(0,0,0)$  and  $\tilde{X}(0,1,0)$ . In addition, a polynomial baseline was fitted, with terms up to quartic in wavelength. This non-zero baseline is mostly due to slow systematic drifts in the lamp spectrum. The best fit simulated spectrum is shown in Fig. 7(b).

The best fit was obtained with  $T_{\text{rot}} = (350 \pm 25)$  K and  $T_{\text{vib}} = (303 \pm 25)$  K. The  $\text{CF}_2$  column density in this outer region was determined to be  $4.9 \times 10^{14}$  molecules/cm<sup>2</sup>, corresponding to a number density of  $(1.5 \pm 0.3) \times 10^{13}$  molecules/cm<sup>3</sup>, taking a column length of 32.6 cm. It should be noted that under normal pumping conditions, the  $\text{CF}_2$  density in this outer region is much lower, as shown in

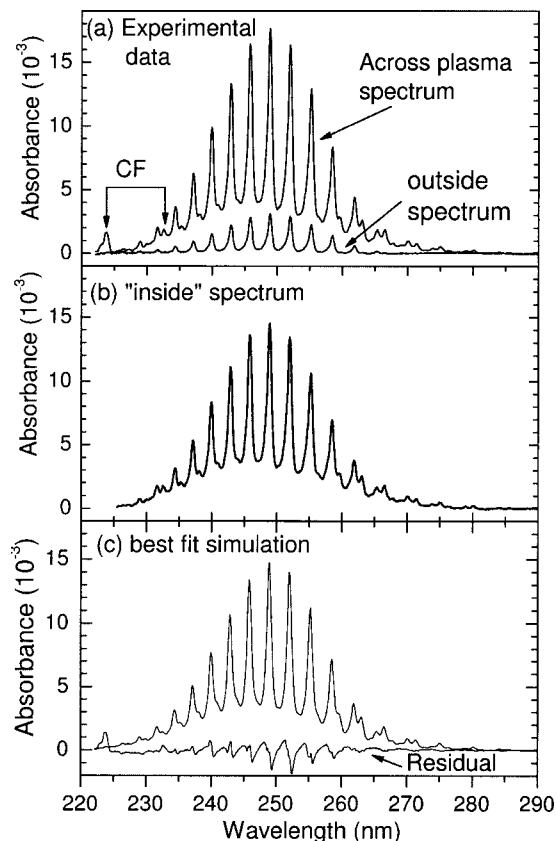


FIG. 8. (a) Experimental spectra of  $\text{CF}_2$ . The lower spectrum is the “outside” spectrum and the upper spectrum is the “across plasma” spectrum. (b) The spectrum of  $\text{CF}_2$  inside the plasma, deduced from the “outside” and “across plasma” spectra. (c) The best-fit simulation and residual of fit.

Fig. 8. In this case, a  $\text{CF}_2$  number density of  $(0.39 \pm 0.8) \times 10^{13}$  molecules/cm<sup>3</sup> was estimated. The principal sources of uncertainty in the density are the uncertainty in the transition dipole moment ( $\pm 10\%$ ), and the uncertainty in the fit. Also shown is the residual of the fit. The intensities of the different vibronic transitions are in good agreement with experiment. The structure in the residual is due to problems fitting the rotational envelope of each band. We attribute this to the use of a 0.45 nm FWHM Gaussian spectral transmission function, when the true function is closer to a trapezoidal function. The consequence of this is increased uncertainty in the rotational temperature: better precision could be obtained from spectra at higher resolution of a single vibronic band.

##### B. Spectra taken across the active plasma

Figure 8(a) shows a spectrum taken across the plasma. This spectrum is very different to the “outside” spectrum (also shown in this case with the turbo pump not throttled), showing an apparent broad continuum of absorption under the band. This difference is due to the higher gas temperature in the confined plasma region. It is necessary to take into account the absorbance due to the  $\text{CF}_2$  present outside the confinement rings, which has a lower gas temperature.

In practice, we subtracted this “outside” contribution with the aid of the spectra taken outside of the rings, assum-

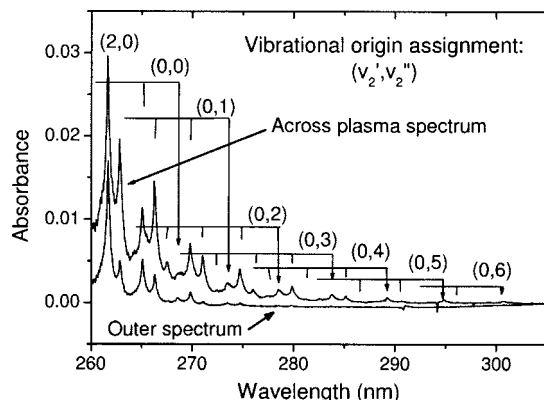


FIG. 9. An assignment of the vibrational hot bands for the CF<sub>2</sub> spectra. The lower spectrum is the outer spectrum while the upper spectrum is the “across plasma” spectrum. Note that this spectrum was taken under conditions with higher CF<sub>2</sub> density, and at higher spectral resolution. The assignments made in this figure are from the results of the simulations.

ing a uniform CF<sub>2</sub> density in this region and correcting for the known pathlength of the UV beam. The resulting “inside” spectrum, representing only the absorption spectrum within the plasma volume, is shown in Fig. 8(b).

Several CFA  $^2\Sigma \leftarrow X^2\Pi$  absorption bands are known to occur at slightly higher energy of the CF<sub>2</sub>  $\tilde{A} \leftarrow \tilde{X}$  absorption band.<sup>9,17</sup> For example, the CFA–X(1,0) band can be seen in Fig. 8(a) at 224 nm and the weaker CFA–X(0,0) band can be seen at 233 nm. The CFA–X(0,0) band does contribute weakly to the experimental “inside” spectrum in Fig. 8(b) at 233 nm, but its presence does not hamper the simulation of the overall envelope obtained in terms of a CF<sub>2</sub> absorption envelope.

Attempts to fit the “inside plasma” spectra assuming Boltzmann equilibrium of the vibrational energy levels (with  $T_{\text{vib}} \approx T_{\text{rot}}$ ) gave poor results. A more detailed analysis of the “across plasma” spectrum in the long-wavelength range (Fig. 9) shows many bands occurring at wavelengths above the band origin at 268 nm, suggesting the presence in the plasma of highly vibrationally excited ground state CF<sub>2</sub> molecules, excited up to six quanta in the  $\nu_2''$  mode. Figure 9 shows the assignment of these bands, based on calculated transition energies and Franck–Condon factors. It should be noted that this spectrum was taken under somewhat different plasma conditions, where the CF<sub>2</sub> density was significantly higher, and that the spectral resolution is also higher in this spectrum.

This suggests that the CF<sub>2</sub> molecules are initially produced in the plasma in highly excited vibrational states and are only partially relaxed by collisions. The presence of these highly vibrationally excited molecules contributes to the apparent continuum absorption observed for the “inside” spectrum. Consequently, to simulate this spectrum, additional ground state levels were included. The rotational constants for these levels were taken from the *ab initio* calculations as listed in Table III.

It should be noted here that, even for such “hot” spectra, it should be possible to deduce the absolute CF<sub>2</sub> density from the *integrated* intensity over all bands, independent of the vibrational level distribution, provided the baseline can be

determined, and there is no other absorbing species present in this spectral region. Based upon the apparent continuum structure often observed in CF<sub>2</sub> absorption spectra, Cruden *et al.*<sup>10</sup> have suggested that there may be an underlying absorption band caused by a molecule other than CF<sub>2</sub>. However, our ability to fit the spectra accurately using only CF<sub>2</sub> transitions (see below) eliminates this uncertainty.

Eleven vibrational levels of the ground state were considered in the fit. A good fit [Fig. 8(c)] was achieved assuming a bi-Maxwellian vibrational energy distribution (47% of the molecules with  $T_{\text{vib}} = 300 \pm 80$  K and 53% with  $T_{\text{vib}} = 1000 \pm 200$  K), and a single rotational temperature of  $500 \pm 100$  K. The estimated CF<sub>2</sub> density in the plasma is  $(3.0 \pm 0.6) \times 10^{13}$  molecules/cm<sup>3</sup>. The rotational temperature is not precise, for the reasons stated above. Indeed, we cannot affirm with certainty whether the rotational distribution is single Maxwellian, due to the inadequate resolution and the severe overlapping of the bands. The higher vibrational temperature is determined with reasonable accuracy from the long-wavelength (>260 nm) region. The lower vibrational temperature is also not determined with precision. *However, it is important to note that the presence of highly vibrationally excited molecules (whose presence is proven by the long-wavelength region) satisfactorily explains the apparent continuum absorption around the band maximum.*

The rotational temperature found for CF<sub>2</sub> is consistent with the rotational temperature determined for CFX  $^2\Pi$  of  $450 \pm 25$  K in the same reactor and comparable plasma conditions.<sup>17,18</sup> The vibrational temperature for CFX  $^2\Pi$  was higher than the rotational temperature and about 850 K. The moderate number of vibrational levels populated for a relatively light diatomic molecule precludes the determination of a bimodal distribution, as has been shown for CF<sub>2</sub> in the present work. The results from both absorption studies confirm the rotational distributions as a good estimate of the gas kinetic energy, while the vibrational distributions tend to give information on excitation mechanisms like electron impact vibrational excitation and exothermicity of the chemical reaction producing the reactive species. Partial relaxation by collisions can be used to explain the lower-temperature component of the vibrational distribution. In any case, additional information is necessary to establish the meaning of the derived vibrational distributions in plasmas of the fluorocarbon reactive species.

## V. CONCLUSIONS

Broadband absorption spectroscopy has been used to study the CF<sub>2</sub>  $\tilde{A} \leftarrow \tilde{X}$  absorption in a plasma etch reactor. This absorption band has been used previously to estimate absolute CF<sub>2</sub> densities (9,17) relying on the absolute CF<sub>2</sub> cross-sections of Sharpe *et al.*<sup>27</sup> This approach leads to significant uncertainty due to the problem of defining the baseline for absorption and allowing for vibrational and rotational excitation in the ground-state CF<sub>2</sub>. Previous estimates of CF<sub>2</sub> vibrational and rotational temperatures have relied on estimated Franck–Condon factors taken from SVL fluorescence measurements. This study represents a major advance in that reliable Franck–Condon factors between low-lying vibra-

ional levels of  $\text{CF}_2 \tilde{X}^1A_1$  to vibrational levels of  $\text{CF}_2 \tilde{A}^1B_1(v'_1, v'_2, 0)$  (with  $v'_1 + v'_2 < 40$ ) were computed using high level *ab initio* calculations combined with an anharmonic Franck-Condon factor method. The Franck Condon factors were used to calculate absorption cross-sections at selected  $\text{CF}_2$  absorption wavelengths, which were then used to calculate number densities.

Spectra were recorded for different regions in the plasma reactor, including regions outside the confined plasma volume and the center of the plasma. For absorption spectra obtained outside the confined plasma volume under conventional running conditions, the  $\text{CF}_2$  density was determined as  $(0.39 \pm 0.08) \times 10^{13}$  molecule  $\text{cm}^{-3}$  and the vibrational and rotational temperatures were determined as  $303 \pm 25$  and  $350 \pm 25$  K, respectively. In the center of the plasma reactor, the  $\text{CF}_2$  density is estimated as  $(3.0 \pm 0.6) \times 10^{13}$  molecules  $\text{cm}^{-3}$  with  $T_{\text{rot}} \approx 500$  K. The fitted vibrational distribution in the  $\text{CF}_2$  ground state corresponds to two Boltzmann distributions with  $T_{\text{vib}} \approx 300$  and  $T_{\text{vib}} \approx 1000$  K, indicating that  $\text{CF}_2$  molecules are initially produced highly vibrationally excited but are partially relaxed in the plasma by collision. This study shows the value of using reliable Franck Condon factors in the analysis of vibrationally resolved absorption spectra recorded for reactive molecules in plasmas. These Franck-Condon factors are not readily available experimentally but can now be calculated with highly accurate *ab initio* multidimensional PEFs.

This study has shown that modern molecular orbital methods can be used to calculate accurate potential surfaces of electronic states involved in an electronic absorption, which can in turn be used to obtain reliable vibrational wave functions and rotational constants up to high vibrational levels in each state. The vibrational wave functions can be used to compute reliable Franck-Condon factors that can then be used to simulate absorption spectra, which include contributions both from the ground vibrational level as well as higher vibrational levels. These hot-band contributions have been found to be particularly important in this present work.

It is proposed to extend this approach to other reactive molecules such as  $\text{SiF}_2$ ,  $\text{HSiF}$ , and  $\text{HCF}$ .

## ACKNOWLEDGMENTS

The authors are grateful to the Research Grant Council (RGC) of the Hong Kong Special Administrative Region

(HKSAR, Grant Nos. AoE/B-10/1, PolyU 5298/01P, and PolyU 5003/03P), the Research Committee of the Hong Kong Polytechnic University of HKSAR (Grant No. G-T635), and the Leverhulme Trust. J.P.B. and N.B. acknowledge financial support from Lam Research Corporation.

- <sup>1</sup>K. Sasaki, H. Furukawa, K. Kudota, and C. Suzuki, *J. Appl. Phys.* **88**, 5585 (2000).
- <sup>2</sup>M. Nakamura, M. Hori, T. Goto, M. Ito, and N. Nishii, *J. Appl. Phys.* **90**, 580 (2001).
- <sup>3</sup>B. K. McMillin and M. R. Zachariah, *J. Vac. Sci. Technol. A* **15**, 230 (1997).
- <sup>4</sup>C. Suzuki, K. Sasaki, and K. Kadota, *J. Vac. Sci. Technol. A* **16**, 2222 (1998).
- <sup>5</sup>G. A. Hebner, *J. Appl. Phys.* **89**, 900 (2001).
- <sup>6</sup>J. P. Booth, *Plasma Sources Sci. Technol.* **8**, 249 (1999).
- <sup>7</sup>G. Cunge and J. P. Booth, *J. Appl. Phys.* **85**, 3952 (1999).
- <sup>8</sup>J. P. Booth, G. Cunge, P. Chabert, and N. Sadeghi, *J. Appl. Phys.* **85**, 3097 (1999).
- <sup>9</sup>J. P. Booth, G. Cunge, F. Neuilly, and N. Sadeghi, *Plasma Sources Sci. Technol.* **7**, 423 (1998).
- <sup>10</sup>B. A. Cruden, K. K. Gleason, and H. H. Sawin, *J. Appl. Phys.* **89**, 915 (2001).
- <sup>11</sup>J. A. O'Neill and J. Singh, *J. Appl. Phys.* **76**, 5967 (1994).
- <sup>12</sup>J. A. O'Neill and J. Singh, *J. Appl. Phys.* **77**, 497 (1995).
- <sup>13</sup>H. Kim and F. L. Terry, Jr., *Proc. SPIE* **3742**, 136 (1999).
- <sup>14</sup>D. S. King, P. K. Schenck, and J. C. Stephenson, *J. Mol. Spectrosc.* **78**, 1 (1979).
- <sup>15</sup>F. T. Chau, J. M. Dyke, E. P. F. Lee, and D. K. W. Mok, *J. Chem. Phys.* **115**, 5816 (2001).
- <sup>16</sup>F. T. Chau, J. M. Dyke, E. P. F. Lee, and D. C. Wang, *J. Electron Spectrosc. Relat. Phenom.* **97**, 33 (1998).
- <sup>17</sup>J. Luque, E. A. Hudson, and J. P. Booth, *J. Chem. Phys.* **118**, 622 (2003).
- <sup>18</sup>J. Luque, E. A. Hudson, J. P. Booth, and I. D. Petsalakis, *J. Chem. Phys.* **118**, 1206 (2003).
- <sup>19</sup>*CRC Handbook of Chemistry and Physics*, 63rd ed., edited by R. C. Weast (CRC, Boca Raton, FL, 1982).
- <sup>20</sup>MOLPRO is a package of *ab initio* programs written by H.-J. Werner and P. J. Knowles; version 2002.1, with contributions from J. Almlöf, R. D. Amos, A. Berning *et al.*
- <sup>21</sup>W. Meyer, P. Botschwina, and P. Burton, *J. Chem. Phys.* **84**, 891 (1986).
- <sup>22</sup>S. Carter and N. C. Handy, *J. Chem. Phys.* **87**, 4294 (1987).
- <sup>23</sup>R. N. Dixon (private communication).
- <sup>24</sup>H. B. Qian and P. B. Davies, *J. Mol. Spectrosc.* **169**, 201 (1995).
- <sup>25</sup>C. W. Mathews, *Can. J. Phys.* **45**, 2355 (1967).
- <sup>26</sup>W. Hack and A. Wilms, *J. Phys. Chem.* **90**, 4007 (1986).
- <sup>27</sup>S. Sharpe, B. Harnett, H. S. Sethi, and D. S. Sethi, *J. Photochem.* **38**, 1 (1987).